Global Diagnostics of Ionospheric Absorption During X-Ray Solar Flares Based on 8- to 20-MHz Noise Measured by Over-the-Horizon Radars

O. Berngardt, J. Ruohoniemi, J.-p. St-maurice, A. Marchaudon, M. Kosch, A. Yukimatu, N. Nishitani, S. Shepherd, M. Marcucci, H. Hu, et al.

Space Weather

RESEARCH ARTICLE
10.1029/2018SW002130

Global Diagnostics of Ionospheric Absorption During X-Ray Solar Flares Based on 8- to 20-MHz Noise Measured by Over-the-Horizon Radars

Berngardt O. I.[1], Ruohoniemi J. M.[2], St-Maurice J.-P.[3], Marchaudon A.[4], Kosch M. J.[5,6,7], Yukimatu A. S.[8,9], Nishitani N.[10], Shepherd S. G.[11], Marcucci M. F.[12], Hu H.[13], Nagatsuma T.[14], and Lester M.[15]

[1]Institute of Solar-Terrestrial Physics, SB RAS, Irkutsk, Russia, [2]Bradley Department of Electrical and Computer Engineering, Virginia Polytechnic Institute and State University, Blacksburg, VA, USA, [3]Department of Physics and Engineering Physics, University of Saskatchewan, Saskatoon, Canada, [4]Research Institute in Astrophysics and Planetology, Toulouse University, CNRS, CNES, Toulouse, France, [5]South African National Space Agency, Hermanus, South Africa, [6]Physics Department, Lancaster University, Lancaster, UK, [7]Department of Physics and Astronomy, University of Western Cape, Bellville, South Africa, [8]National Institute of Polar Research, Tokyo, Japan, [9]School of Multidisciplinary Sciences, Department of Polar Science, The Graduate University for Advanced Studies (SOKENDAI), Tokyo, Japan, [10]Institute for Space-Earth Environmental Research, Nagoya University, Nagoya, Japan, [11]Thayer School of Engineering, Dartmouth College, Hanover, NH, USA, [12]Institute for Space Astrophysics and Planetology, Rome, Italy, [13]Polar Research Institute of China, Shanghai, China, [14]National Institute of Information and Communications Technology, Tokyo, Japan, [15]Department of Physics and Astronomy, University of Leicester, Leicester, UK

Key Points:
- HF noise attenuation in the ionosphere was investigated with 35 radars during 80 X-ray solar flares
- The evolution of HF noise attenuation following an X-ray solar flare is explained by a linear combination of 1- to 8- and 94-$\AA$ solar radiation
- The experimental frequency dependence of the absorption at 8–20 MHz is $A[dB] \sim f^{-1.6}$

Supporting Information:
- Supporting Information S1

Correspondence to:
O. I. Berngardt,
berng@iszf.irk.ru

Citation:
Berngardt, O. I., Ruohoniemi, J. M., St-Maurice, J.-P., Marchaudon, A., Kosch, M. J., Yukimatu, A. S., et al. (2019). Global diagnostics of ionospheric absorption during X-ray solar flares based on 8- to 20-MHz noise measured by over-the-horizon radars. *Space Weather*, *17*, 907–924. https://doi.org/10.1029/2018SW002130

Received 28 NOV 2018
Accepted 28 APR 2019
Accepted article online 2 MAY 2019
Published online 24 JUN 2019

Abstract An analysis of noise attenuation during 80 solar flares between 2013 and 2017 was carried out at frequencies 8–20 MHz using 34 Super Dual Auroral Radar Network radars and the EKB ISTP SB RAS radar. The attenuation was determined on the basis of noise measurements performed by the radars during the intervals between transmitting periods. The location of the primary contributing ground sources of noise was found by consideration of the propagation paths of radar backscatter from the ground. The elevation angle for the ground echoes was determined through a new empirical model. It was used to determine the paths of the noise and the location of its source. The method was particularly well suited for daytime situations, which had to be limited for the most part to only two crossings through the *D* region. Knowing the radio path was used to determine an equivalent vertical propagation attenuation factor. The change in the noise during solar flares was correlated with solar radiation lines measured by GOES/XRS, GOES/EUVS, SDO/AIA, SDO/EVE, SOHO/SEM, and PROBA2/LYRA instruments. Radiation in the 1 to 8 $\AA$ and near 100 $\AA$ are shown to be primarily responsible for the increase in the radionoise absorption, and by inference, for an increase in the *D* and *E* region density. The data are also shown to be consistent with a radar frequency dependence having a power law with an exponent of −1.6. This study shows that a new data set can be made available to study *D* and *E* regions.

1. Introduction

The monitoring of ionospheric absorption at high frequency (HF), particularly at high latitudes, makes it feasible to predict radio wave absoption at long distances and therefore on global scales (Akmaev, 2010; DRAP Documentation, 2010). This in turn makes it a useful tool for study of the dynamics of the *D* and *E* regions. Traditionally, there are several techniques in use (Davies, 1969; Hunsucker & Hargreaves, 2002), including constant power 2- to 6-MHz transmitters (URSI A1 and A3 methods; see, e.g., Sauer & Wilkinson, 2008; Schumer, 2010), riometry using cosmic radio space sources at 30–50 MHz (URSI A2 method; Hargreaves, 2010), and imaging riometry (Detrick & Rosenberg, 1990). Recently, a large, spatially distributed network of riometers has been deployed to monitor absorption (Rogers & Honary, 2015). The development of new techniques for studying absorption with wide spatial coverage would be valuable for the validation of global ionospheric models and for global absorption forecasting.

A wide network of radio instruments in the HF range is available with the SuperDARN (Super Dual Auroral Radar Network; Greenwald et al., 1995; Chisham et al., 2007) radars and radars close to them in terms of design and software (Berngardt et al., 2015). The main task of the SuperDARN network is to measure iono-

spheric convection. Currently, this network is expanding from polar latitudes to midlatitudes (Baker et al., 2007; Ribeiro et al., 2012) and possibly to equatorial latitudes (Lawal et al., 2018). Regular radar operation with high spatial and temporal resolutions and a wide field of view makes them a useful tool for monitoring ionospheric absorption on global scales. The frequency range used by the radars fills a gap between the riometric measurements at 30–50 MHz (URSI A2 method) and radar measurements at 2- to 6-MHz band (URSI A1 and A3 methods). Various methods are being developed for using these radars to study radio wave absorption. One approach is to monitor third-party transmitters (Squibb et al., 2015) and another is to use the signal backscattered from the ground (Chakraborty et al., 2018; Fiori et al., 2018; Watanabe & Nishitani, 2013). In this paper, another method is investigated. It is based on studying the attenuation of HF noise in the area surrounding the radar that is measured without transmitting any sounding pulses.

Every several seconds, before transmitting at the operating frequency, the radar measures the spectrum of the background noise in a 300- to 500-kHz band centered on a planned operating frequency that lies between 8 and 20 MHz. The minimum in the spectral intensity is recorded and defined here as the "minimal HF noise level."

Berngardt et al. (2018) showed that the dynamics of the minimal HF noise level is strongly influenced by X-ray 1- to 8-$\AA$ solar radiation in the daytime. This effect has also been observed during solar proton events (Bland et al., 2018) where it was found to correlate well with riometer observations. This allows one to use the noise measured with HF radars to investigate the absorption processes in the lower part of the ionosphere in passive mode, without the use of third-party transmitters, and without relying on the presence of backscatter from the ground.

To use this new technique on a regular basis for monitoring ionospheric absorption, we should investigate the observed noise level variations during X-ray flares and show that the observed dynamics are consistent with the current absorption models.

As shown in the preliminary analysis (Berngardt et al., 2018), there is significant correlation of noise level attenuation with the intensity of X-ray solar radiation in the range 1–8 $\AA$. However, the temporal dynamics of the absorption sometimes do not precisely track the solar radiation at wavelengths of 1–8$\AA$, which indicates the presence of mechanisms other than the ionization of the *D* layer by 1- to 8-$\AA$ solar radiation. An example of such a comparison will be presented here in Figures 1a–1d and was shown by Berngardt et al. (2018, Figure 9).

In contrast to riometers, which measure ionospheric absorption at relatively high frequencies (30–50 MHz), the SuperDARN coherent radars use lower operating frequencies and ionospheric refraction significantly affects the absorption level—the trajectory of propagation is distorted by the background ionosphere. To compare the data of different radars during different solar flares, our method requires taking into account the state of the background ionosphere during each experiment. This allows an oblique absorption measurement to be converted to an equivalent vertical measurement. In addition, the solution of this problem allows determination of the geographic location of the region in which the absorption takes place.

Among the factors that affect the error in estimating the absorption level is the frequency at which the radar operates and its irregular switching. It is known that the absorption of radio waves depends on frequency, but this dependence is taken into account in different ways in different papers. In order to make a reliable comparison of data collected from radars operating at different frequencies, it is necessary to find the frequency dependence of the HF noise absorption, and to take it into account. This will allow us to infer the absorption at any frequency from the observed absorption at the radar operating frequency.

The third factor that needs to be taken into account is the altitude localization of the absorption.

The present paper is devoted to solving these problems. An analysis is made of 80 X-ray solar flares during the years 2013–2017, which were also considered in (Berngardt et al., 2018) based on the available data of 34 high- and middle-latitude radars of SuperDARN network and on the EKB ISTP SB RAS (Berngardt et al., 2015) radar data. The radar locations and their fields of view are shown in Figures 1e and 1f; the radar coordinates are given in the Table S1 (supporting information). The X-ray solar flares dates are listed in Berngardt et al. (2018).

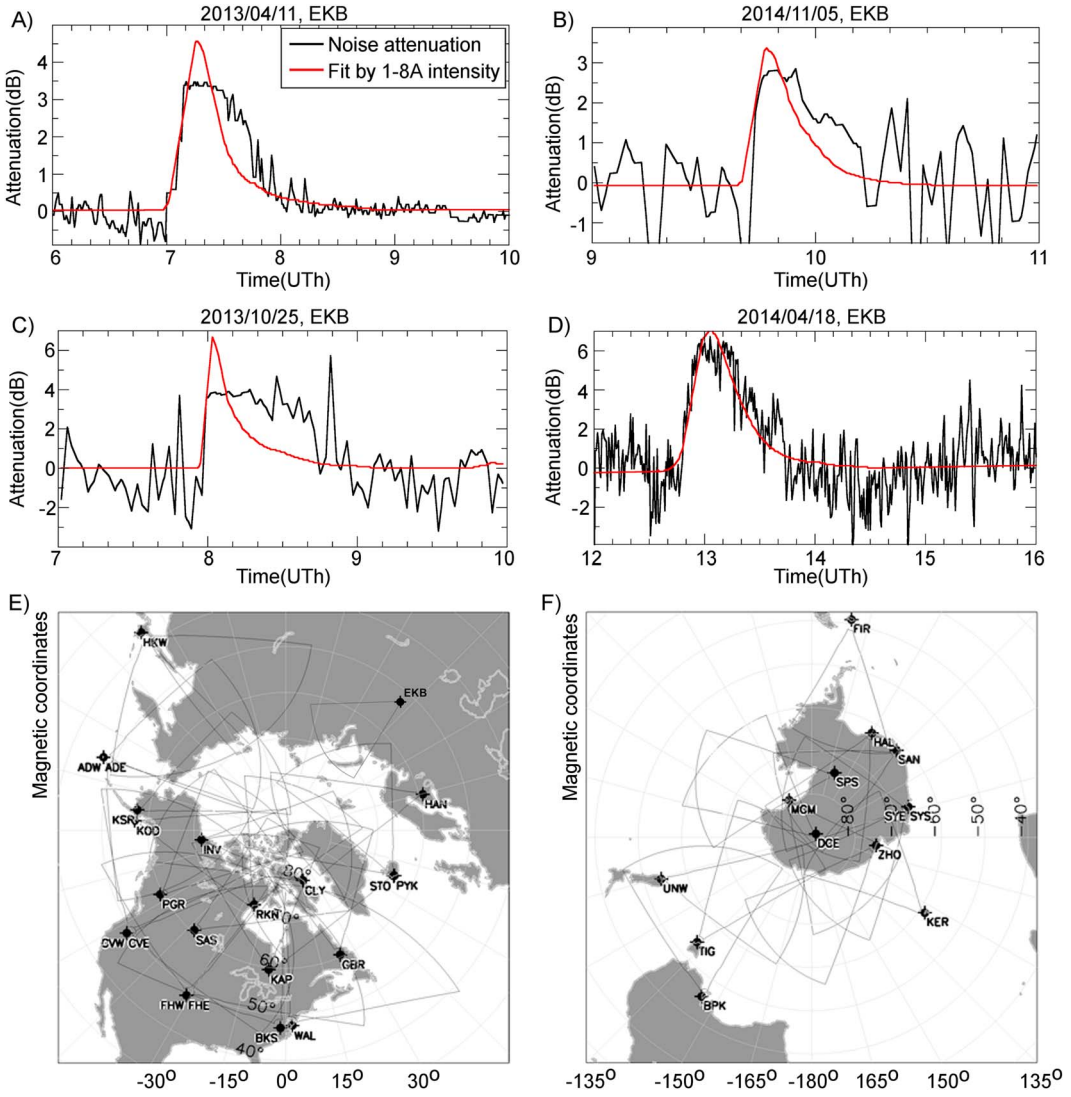

Figure 1. (a–d) Comparison of the X-ray intensity dynamics measured on GOES/XRS 1–8 $\AA$ and the noise attenuation at EKB ISTP SB RAS radar during four flares; (e–f) fields of views of radars that participated in the work.

2. Taking Into Account the Background Ionosphere

As was shown in Berngardt et al. (2018), during solar X-ray flares, attenuation of the minimal noise level in the frequency range 8–20 MHz is observed on the dayside by midlatitude coherent radars. The attenuation correlates with the increase of X-ray solar radiation 1–8 $\AA$ and is associated with the absorption of the radio signal in the lower part of the ionosphere.

The HF radio noise intensity is known to vary with local time due to different sources (ITU-R P.372-13, 2016). At night, the noise is mostly atmospheric and is formed by long-range propagation from noise sources around the world, mostly from regions of thunderstorm activity. In the daytime the atmospheric noise level significantly decreases due to regular absorption in the lower part of the ionosphere and the increasing number of propagation hops (caused by increasing electron density and lowering of the radio wave reflection point). As a result, in the daytime the multihop propagation part of the noise becomes small, and only noise sources from the first propagation hop (mostly anthropogenic noise) need to be taken into account (Berngardt et al., 2018).

An important issue related to the interpretation of the noise level is the spatial localization of the effect. It can be estimated by taking into account the radio wave trajectory along which most of the noise is received and absorption is taking place. We will argue that ionization of the lower ionosphere is small enough and skip

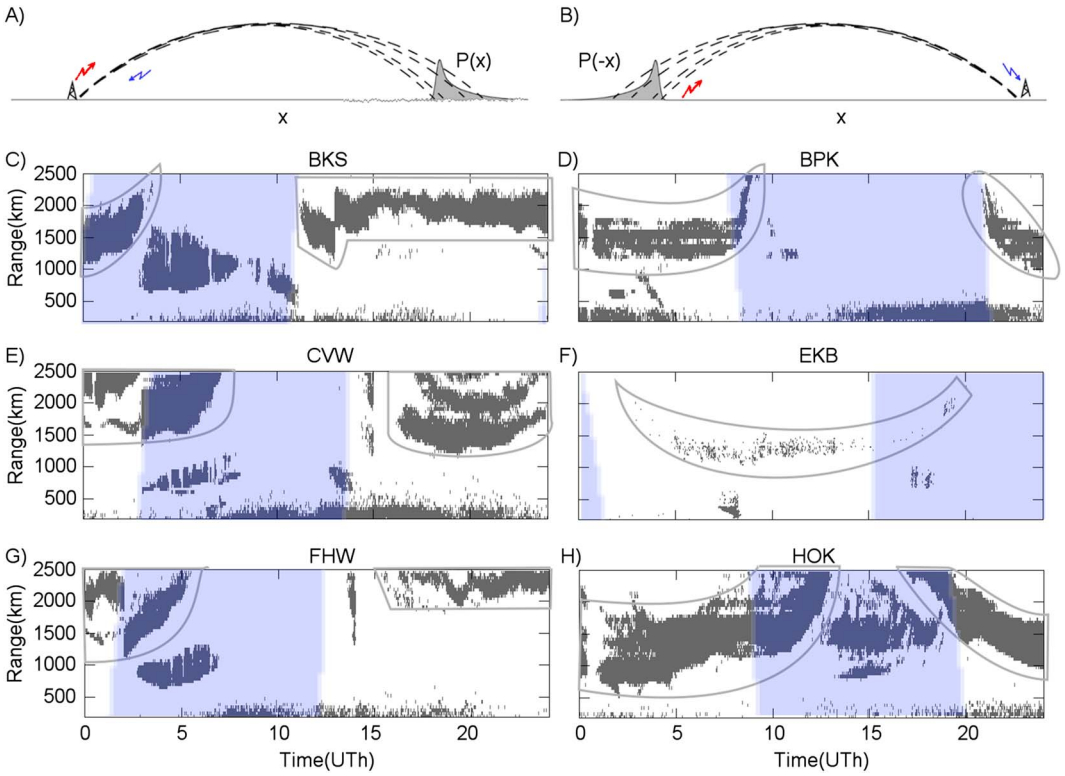

Figure 2. (a) Formation of GS signal; (b) formation of noise power level by distribution of noise sources. Red and blue arrows in (a) and (b) mark transmitted and received signals; (c–h) the position of the signals, defined by FitACF algorithm as GS, during 18 April 2016 on the radars BKS, BPK, CVW, EKB, FHW, and HOK. Gray enclosed areas correspond to GS when focusing in the *F* layer. Other areas are defined by the algorithm, as GS, but having, sometimes, an ionospheric origin. Blue areas marks unlit conditions. GS = ground scatter.

distance variability is less pronounced than the variations caused by other regular and irregular ionospheric variations.

Let us consider the problem of detecting the noise source from the data of a HF coherent radar. It is known that the intensity of the signal transmitted by an isotropic source and propagating in an inhomogeneous ionosphere substantially depends on the ground distance from the signal transmitter to receiver. If we consider only waves reflecting from the ionosphere, then at sounding frequencies above *foF*2 there is a spatial region where the signal cannot be received - the dead zone. At the boundary of this dead zone (skip distance) the signal appears and is significantly enhanced compared to other distances (Bliokh et al., 1988; Shearman, 1956).

In the first approximation the power of the scattered signal received by the radar will be proportional to the product of (i) the power of the incident signal $P(x)$ (related to spatial focusing when propagating from the radar to the Earth's surface); (ii) the scattering cross section $\sigma(x)$ (related to inhomogeneities of the Earth's surface); and (iii) the incident power $P(x)$ (related to the propagation from the Earth's surface to the radar).

This signal is received as a powerful signal coming from a small range of distances (about several hundreds kilometers). When analyzing the data of coherent HF radars, this signal, associated with the focusing of the radio wave at the boundary of the dead zone, is referred to as ground scatter (GS; Shearman, 1956). The process of forming the GS signal is illustrated in Figure 2a.

The scattering cross section $\sigma(x)$ essentially depends on the angles of incidence and reflection of the wave, as well as on the properties and geometry of the scattering surface. This causes a significant dependence of the GS signal on the landscape and the season (Ponomarenko et al., 2010). In the case of presence of significant inhomogeneities, for example, mountains (Uryadov et al., 2018), $\sigma(x)$ may cause the appearance of additional maxima and minima in the GS signal. For relatively homogeneous surfaces, the position of the GS maximum remains almost unchanged, and the GS signal propagation trajectory (radar-surface-radar)

can be used to estimate the trajectory of the propagation of the noise signal (surface-radar). The process of forming the received signal is illustrated in Figure 2b.

Thus, the problem of localization of the noise source can be reduced to determining the geographic location of the region forming the GS signal and determining the propagation path of the signal from this region to the receiver. Below we use this approximation to localize noise source using GS signal properties.

The study of absorption on the long paths using GS signal or noise requires knowledge of the trajectory of radio space signal propagation especially in the two regions where it intersects the *D* layer—near the receiver (radar) and near the transmitter source (point of focusing, where the GS signal is formed). According to the Breit-Tuve principle (Davies, 1969), it is sufficient to know the angle of arrival of the GS signal and the radar range. In practice, however, there are two significant problems: the separation of the GS signal from the ionospheric scatter signal (Blanchard et al., 2009; Ribeiro et al., 2011) and the calibration of the arrival angle measurements (Chisham, 2018; Ponomarenko et al., 2015; Shepherd, 2017).

Figures 2c–2h present examples of the location of signals detected as GS by the standard FitACF algorithm (used on these radars for signal processing). It can be seen from the figure that the scattered signal can include several propagation paths (Figure 2e, 16–24 UT), variations in the GS signal range (associated, for example, with the propagation of internal atmospheric waves; Oinats et al., 2016; Stocker et al., 2000; Figure 2c, 14–18 UT; Figure 2g, 18–21 UT), as well as ionospheric and meteor trail scattering (Figures 2c–2h, ranges below 400 km; Hall et al., 1997; Ponomarenko et al., 2016; Yukimatu & Tsutsumi, 2002). The signal that qualitatively corresponds to *F* layer GS is marked at Figures 2c–2h by enclosed regions (the modeling results demonstrating this will be shown later in the paper). These examples demonstrate that the problem of stable and automatic selection of the GS region associated with reflection from the *F* layer is rather complicated even with use of the standard processing techniques.

In this study, the position of the *F* layer GS signal was solved for each radar beam separately and independently using an empirical ionospheric model. To generate input data for the GS positioning algorithm for each moment, we identify the ranges where the signals have the maximum amplitude in the radar data. For this purpose we select only signals determined by the standard FitACF algorithm to be GS signal.

Using these prepared input data, we determine the smooth curve of the distribution of GS with range, within the framework of an empirical ionospheric model with a small number of parameters, adapted to the experimental data. The problem of determining the position of the GS signal causes certain difficulties connected to the presence of a large number of possible focusing points associated with the heterogeneity of the ionosphere along the signal propagation path (Stocker et al., 2000) and ionospheric scattered signals incorrectly identified as GS signals.

For an approximate single-valued solution of this problem, we reformulate the problem as the problem of producing a GS signal in a plane-layered ionosphere with a parabolic layer with parameters estimated from the GS signal. In the framework of the plane-layered ionosphere with a parabolic *F* layer, we have the following expression for the radar range to the boundary of the dead zone (Chernov, 1971):

$$R_{\text{model}} = \frac{f_0}{f_{oF2}} \left\{ 2h_{mF2}\sqrt{\chi} + \Delta h \cdot ln\left(\frac{1+\sqrt{\chi}}{1-\sqrt{\chi}}\right)\right\} \tag{1}$$

where $\chi = \frac{h_{mF2}-\Delta h}{h_{mF2}}$; $h_{\min} = h_{mF2} - \Delta h$- is the minimal height of the ionosphere, obtained from the condition $N_e(h_{\min}) = 0$; h_{mF2} is the height of the electron density maximum in the ionosphere, obtained from the condition $N_e(h_{mF2}) = \max$; f_{oF2} is the plasma frequency of the F2 layer; f_0 is the carrier frequency of the sounding signal.

In this model, the geometric distance *D* over the Earth surface to the point of focusing is defined as (Chernov, 1971)

$$D_{\text{model}} = R_{\text{model}} \cos(\Theta_{\text{model}}) \tag{2}$$

The elevation angle Θ_{model} of the signal arriving from the dead zone boundary according to this model is calculated as

$$\cos(\Theta_{\text{model}}) = \sqrt{1 - \chi\left(\frac{f_0}{f_{oF2}}\right)^{-2}} \tag{3}$$

The reference ionospheric model IRI (Bilitza et al., 2017) is a median model and sufficiently smooth in time, but by default, it does not correctly describe fast changes of *foF*2 in some situations, especially at high latitudes (Blagoveshchenskii et al., 2015). This problem becomes especially critical for GS signal range calculations for sunset and sunrise periods. Searching for one or several IRI parameters that are constant during the day will not solve the problem, so it is necessary to use either an adaptive model that more adequately describes these periods, or to use IRI model corrected for each moment using data from an ionosonde network (Blagoveshchenskii et al., 2015; Galkin et al., 2012). We use an adaptive model, which is easier to implement and does not require additional data and instruments.

The adaptive model of the parabolic layer ionosphere was used with a nonlinear model for $foF2(t)$ and constant values for h_{mF2} and Δh:

$$f_{oF2}(t) = f_{oF2,\min} + \left(f_{oF2,\max} - f_{oF2,\min}\right)\varepsilon(t) \tag{4}$$

$$\varepsilon(t) = \frac{\operatorname{atan}\left(\beta \cdot (\Theta(t - \Delta T) - \alpha)\right) - \operatorname{atan}\left(\beta \cdot \left(\Theta_{\min} - \alpha\right)\right)}{\operatorname{atan}\left(\beta \cdot \left(\Theta_{\max} - \alpha\right)\right) - \operatorname{atan}\left(\beta \cdot \left(\Theta_{\min} - \alpha\right)\right)} \tag{5}$$

where $\Theta(t)$ is the cosine of the solar zenith angle at the radar location as a function of the time t; $\Theta_{\min}, \Theta_{\max}$ is the maximal and minimal cosine of the solar zenith angle during the day; $\alpha, \beta, \Delta T$ are modeled parameters, computed during the fitting procedure. More correctly, solar zenith angle should be calculated at the point of radio wave absorption, but in this paper we do not use this. The parameter ΔT compensates the difference in the first approximation.

When searching for optimal parameters of the model (1), the constant height of the maximum h_{mF2} and the half-thickness of the parabolic layer Δh were assumed to be 350 km and 100 km, respectively.

To improve the accuracy of the approximation, a special fitting method has been developed to detect GS signal smooth dynamics in the presence of signals not described by the GS model. The fitting method consists of three stages. At the first stage, the preliminary fitting of the model is made. This stage is required for preliminary rejection of ionospheric scattering and possible additional modes of propagation. At the second stage, we reject those signals, which differ significantly by range from the model. At the third stage, the final fitting of the model is made. During the first and third stages, a genetic algorithm is used (Simon, 2013), as a method of searching for an optimum, but with different input data and with different functionals of the optimum. At the second stage a kind of cluster analysis (Bailey, 1994) is used. The program code is available at Berngardt (2019).

An illustration of the algorithm operation is shown in Figures 3a–3f. All the signals defined by FitACF algorithm as GS signal are shown in gray. The signals defined in the second stage as GS signals are shown by blue crosses in the Figures 3a–3f; other signals are rejected at this stage and marked in the Figures 3a–3f by violet circles. The black lines represent the model dynamics of the GS signal range calculated at the third stage. The line can be discontinuous due to changes of radar operational frequency or night propagation conditions. The good correspondence between the blue dots and black line demonstrates that qualitatively the technique fits the GS radar range quite well in different cases. This indicates a generally good stability of the technique.

In Figures 3a–3f one can also see conditions for which the algorithm does not work well. This happens when ionospheric scattering appears at distances that are close to the daytime GS distance (Figure 3e, 00–03, 12–17 UT; Figure 3f, 15–19 UT). Since X-ray solar flares effects are observed mostly during the day (Berngardt et al., 2018), the nighttime areas are not statistically important for this paper. So we do not pay attention to possible nighttime model range errors. A more critical problem is the case when the first and second hop signals (Figure 3b, 17–24 UT) are observed equally clearly and with nearly the same amplitude. So the model signal is forced to pass in the middle between these tracks. In this case, a significant regular error appears. For a small number of validated data points (Figure 3d), the algorithm can fail too.

The model results have been compared with measurements made by the polar cap (CLY), subauroral (KER), and midlatitude (CVE) radars on 18 April 2016. The root-mean-square (RMS) error between the model elevation angle and the experimental measurements calculated from the interferometric data is 6–9°, with an average error of 1–3° (Figure 3g). The RMS error between the model GS range and the experimental

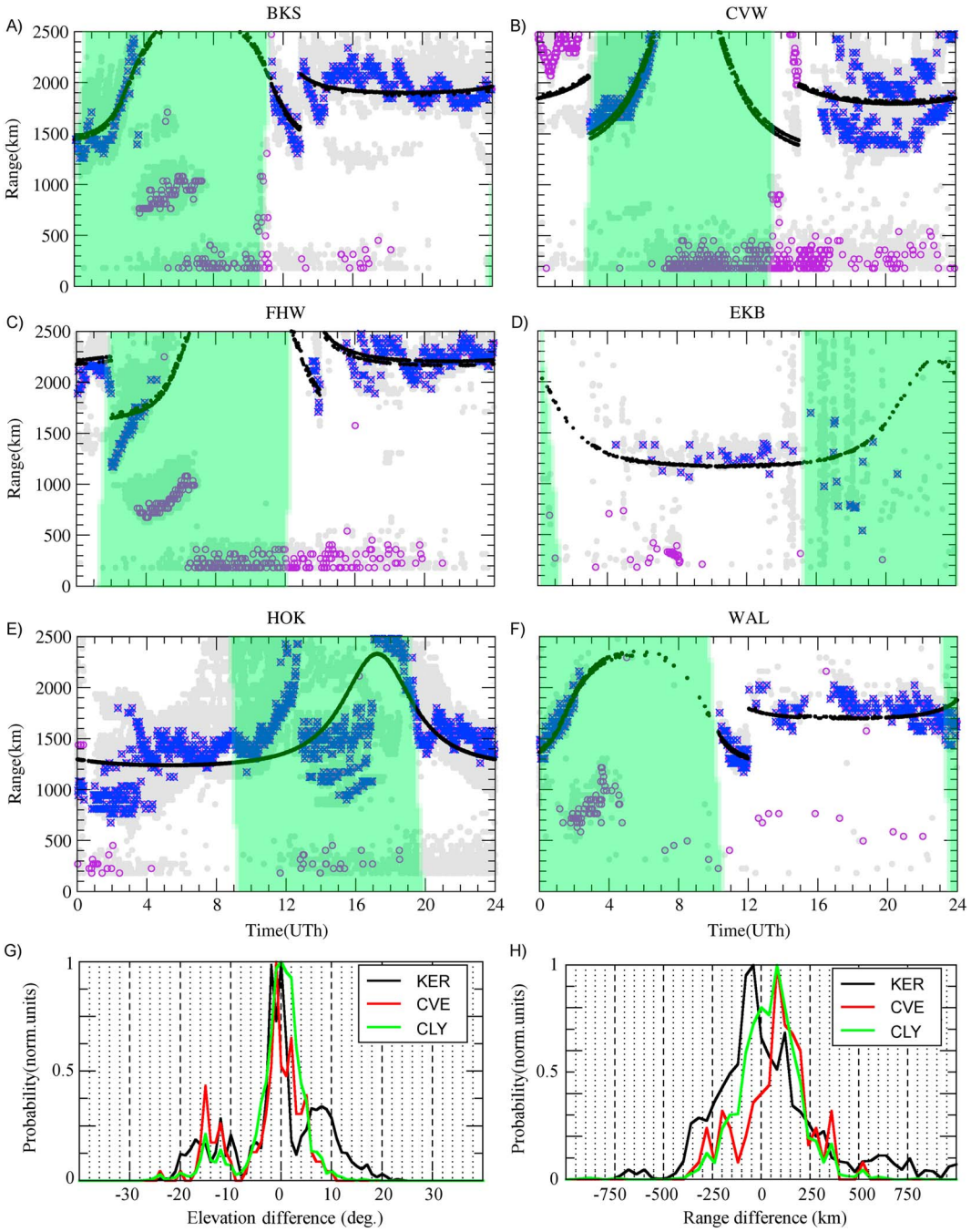

Figure 3. (a–f) Illustration of the work of the fitting technique on various radars during 18 April 2016. Violet: non-GS data, detected at the second stage; blue: GS data, used for third stage; black: GS distance, detected at third stage. Green areas mark unlit conditions. (g) The distribution of difference between model and measured GS elevation angles according to the KER, CVE, and CLY radar data 18 April 2016. (h) The distribution of difference between model and measured GS range according to KER, CVE, and CLY radar data 18 April 2016.

measurements calculated for 18 April 2016 for these radars is 166–315 km, with an average error of 7–47 km (Figure 3h). The comparison shows that the technique can be used for processing polar cap, subauroral, and midlatitude radar data.

In conclusion, in most cases, the algorithm works well enough to enable proper statistical conclusions. The smallness of the average range and elevation angle errors make it possible to use this technique for determining the model GS to carry out statistical studies on a large volume of experimental radar data.

Finally, to identify which hop produces most of the noise absorption, we analyzed the cases when the first hop and second hop GS signal locations are at opposite sides of the solar terminator (i.e., in lit and unlit regions). We studied only cases when the noise absorption correlates well with X-rays at 1–8 Å. The second hop GS distance was estimated by doubling the first hop GS distance (2). This allows us to estimate the geographical location of second hop GS region. Since the absorption correlating with X-rays is mainly associated with the sunlit area (Berngardt et al., 2018), the studied cases allow us to statistically identify the (lit) hop of most effective absorption. For the ≈400 cases found with the correlation coefficient $R > 0.6$ the probability of the absorption at the first hop is 78%. For the ≈70 cases found with $R > 0.9$ the probability of absorption at the 1st hop is 95.5%.

We made a similar comparison of the point above the radar and the point near the edge of the GS region. Our analysis has shown that the probability of absorption near GS region for $R > 0.8$ (over 15 cases) is 54%, for $R > 0.85$ (over 10 cases) is 75% , and for $R > 0.9$ (over four cases) is 100%.

Therefore, in most situations, the daytime noise absorption can be interpreted as absorption on the first hop, with the most probable location near the dead zone.

3. Dependence of the Absorption on the Sounding Frequency

Using the model of the GS signal range described above, it is possible to automatically estimate the elevation angle of the incoming noise signal and, thereby, to transform the oblique absorption to the vertical absorption. Knowing the height of the absorbing region and the range to GS, it is possible to estimate the geographical position of the absorbing region.

Another important factor that needs to be taken into account is the frequency dependence of the absorption. Using it, one can interpolate the absorption measured at the radar operating frequency to the absorption at a fixed frequency. At present, several variants of absorption frequency dependence are used in the analysis of experimental data and forecasting. The DRAP2 model (Akmaev, 2010; DRAP Documentation, 2010) and some nowcast PCA models (Rogers & Honary, 2015) use a frequency dependence given by $A[dB] = A_0 f^{-1.5}$, based on Sauer and Wilkinson (2008). A frequency dependence $A = A_0 f^{-1.24}$ is proposed in Schumer (2010). From the theory of propagation of radio waves, the frequency dependence for sufficiently high probing frequencies exceeding the collision frequency $2\pi f \gg \nu$ absorption should have the dependence $A = A_0 f^{-2}$ (Davies, 1969; Hunsucker & Hargreaves, 2002). Computational models like (Eccles et al., 2005; Pederick & Cervera, 2014) use an ionospheric and a radio wave propagation model to calculate the absorption on each particular path and do not use an explicit frequency dependence.

To perform a comparative statistical analysis on a larger radar data set, it is necessary to retrieve the experimental dependence of the absorption on the frequency of the radar. To determine this dependence, a correlation analysis of the absorption at various frequencies was carried out. We selected "multifrequency experiments," that is, experiments for which, during 6 min, a certain radar simultaneously operated at least on two frequencies, separated by at least 10%, at the same azimuth. After selecting these experiments we built regression coefficients between the noise levels at different frequencies for each "multifrequency experiment," taking into account the possibility of different background noise levels and their various (linear) time dependencies. Thus, the regression coefficient A_0 for each multifrequency experiment was determined as the value minimizing the RMS deviation of noise attenuation $P_1(t), P_2(t)$ at frequencies f_1, f_2 respectively. In other words, A_0 is defined as the solution to the problem:

$$\Omega = \int_{T_{\text{flare}}-1h}^{T_{\text{flare}}+2h} \left(P_1(t)[\text{dB}] - \left\{A_0 P_2(t)[\text{dB}] + A_1 + A_2 t\right\}\right)^2 \text{d}t = \min \tag{6}$$

The integration was made over the regions $P_1(t) < 0.9 \cdot \max(P_1), P_2(t) < 0.9 \cdot max(P_2)$ to exclude noise saturation effects from consideration. To increase the validity of the retrieved data, we analyzed only the cases where the correlation coefficient between the noise attenuation and the variations of the intensity of solar radiation in the 1- to 8-Å band exceeded 0.4, which indicates a statistically significant absorption effect (Berngardt et al., 2018). As a result, we obtained a statistical distribution of the exponent of the power law dependence of the absorption on the frequency

$$A[\text{dB}] \sim f^{-\alpha} \tag{7}$$

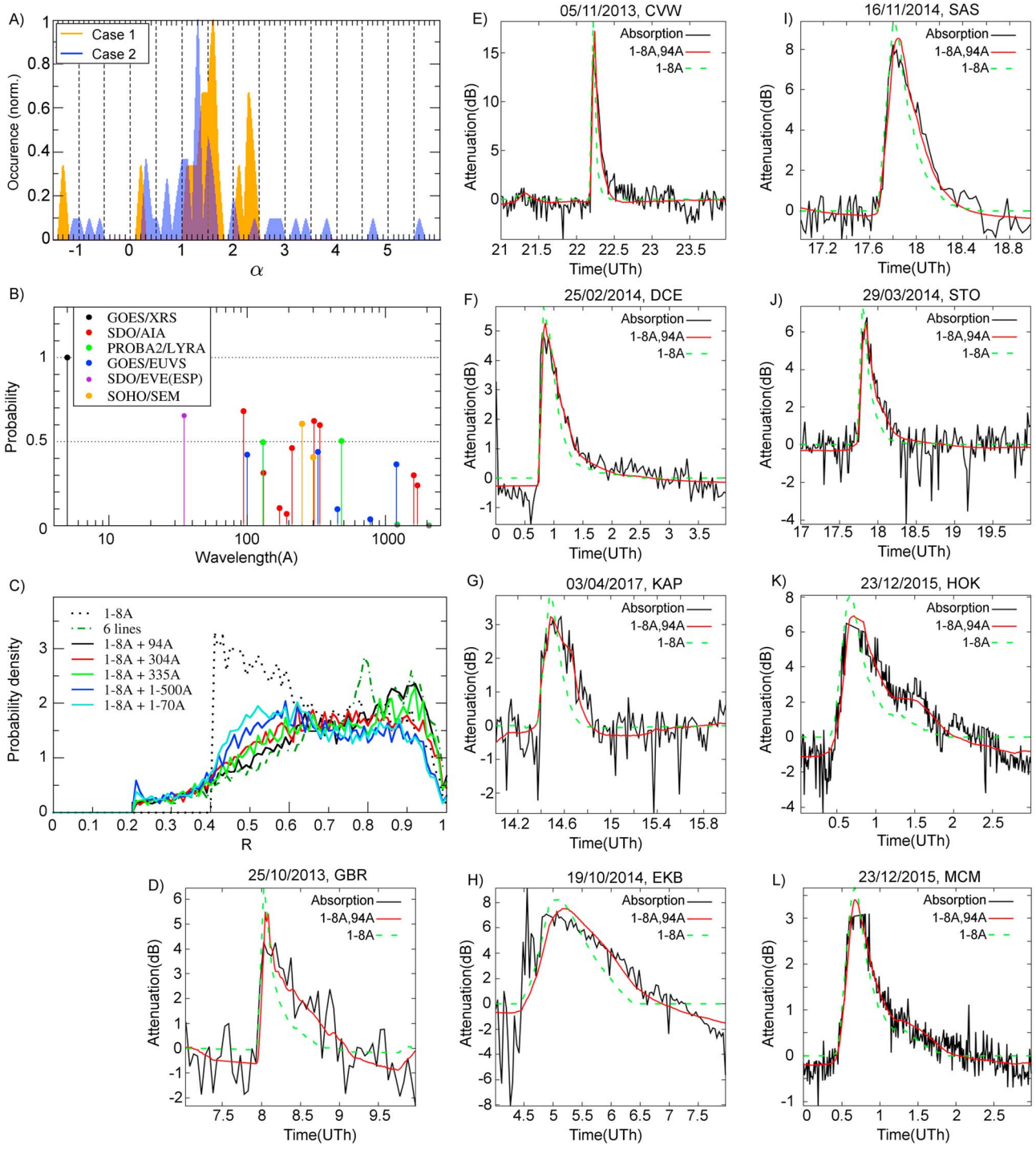

Figure 4. (a) Distributions of the power law (7) coefficient α of the absorption frequency dependence during multifrequency experiments. The two cases (orange and blue) are described in the text and correspond to different data sets and approaches of calculating α; (b) the probability $P(\Lambda)$ (10) over all the flares and the radars; (c) probability density function of correlation coefficients for various approximations of the noise absorption experimental data; (d–l) examples of fitting the attenuation of high-frequency noise by different combinations of solar spectrum lines (at different radars during different X-ray flares).

by calculating the ratio for every experiment:

$$\alpha_i = \frac{log(A_{0,i})}{log(f_{1,i}/f_{2,i})} \tag{8}$$

where $f_{2,i}$,$f_{1,i}$ are the frequencies of noise observation simultaneously on the same beam at the same radar, and $A_{0,i}$ is the coefficient of regression between the absorption and X-ray flare dynamics at different sounding frequencies; i is the experiment number.

Figure 4a shows statistical distributions of α calculated over multifrequency experiments for the cases of highly correlating ($|R| > 0.4$) absorption with 1- to 8-Å solar radiation. To improve the estimates, we selected only experiments with small carrier frequency variations $\delta f_1, \delta f_2$ during flare observations ($|\delta f_1|, |\delta f_2| < 150kHz$) around the average sounding frequencies (f_1,f_2). In other words, we investigated multifrequency experiments with a large enough difference between two frequencies, that is, we required

$$|f_1 - f_2| > 3 \cdot (|\delta f_1| + |\delta f_2|) \tag{9}$$

This final distribution corresponds to 1,662 individual experiments at 18 different radars (BKS, BPK, CLY, DCE, EKB, GBR, HKW, HOK, INV, KAP, KOD, KSR, MCM, PGR, RKN, SAS, TIG, and WAL).

Using this data set, we estimated α by two approaches. The first case is limited by relatively HF difference ($f_1/f_2 \geq 1.5$). In this case α is calculated from the linear regression coefficient between absorption dynamics at two different frequencies. The resulting distribution consists of 15 separate experiments and is shown in Figure 4a by the orange color. The average α and RMS are 1.6 and 0.3 correspondingly.

The second case is limited by cases of high absorption (more than 15 dB) at both frequencies. In this case α is calculated from the relation of peak absorption at both frequencies. The resulting distribution of α consists of 48 separate experiments and is shown in Figure 4a by blue color. The average α and RMS are 1.5 and 0.8 correspondingly.

As one can see, both approaches leads to very similar estimates of α between 1.5 and 1.6. We will use 1.6 obtained in the first case due to the smaller RMS. More accurate calculations of α requires more dual-frequency measurements at the radars.

So the dependence of the absorption on the frequency in the range 8–20 MHz can be described more stably by the empirical dependence $A[\text{dB}] \sim f^{-1.6}$, which is close to $\alpha = 1.5$, used in the conventional absorption forecast model DRAP2 (Akmaev, 2010; DRAP Documentation, 2010). Therefore, we will use the empirically found value $\alpha = 1.6 \pm 0.3$ in the following work.

4. Correlation of Absorption Dynamics With Solar Radiation of Different Wavelengths

The next important issue arising in the investigation of noise data by coherent radars is the interpretation of the detailed temporal dynamics of the noise absorption. As shown in Berngardt et al. (2018) and seen in Figures 1a–1c, the front of noise absorption at the radar correlates well with the shape of the X-ray flare according to GOES/XRS 1–8 Å. The rear is substantially delayed with respect to the X-ray 1- to 8-Å flare. As the preliminary analysis showed, this is a relatively regular occurrence for the data from 2013 to 2017. Since the absorption from the rear is delayed for tens of minutes, it cannot be explained only in terms of recombination in the ionized region.

One possible explanation for the delay in the rear is the contribution to ionospheric absorption of regions higher than the D layer, ionized by solar radiation lines other than the X-ray 1–8 Å. It is known that the lower part of the ionosphere (layers D and E) is ionized by wavelengths <100 Å (Banks & Kockarts, 1973) as well as by Lyman-α line (about 1,200 Å). Most often, researchers analyze the association of absorption with X-ray radiation 1–8 Å only, measured by GOES/XRS and associated with the ionization of the D layer (Rogers & Honary, 2015; Warrington et al., 2016), see Figure 1d. However, the absorption is important not only in the D layer but also in the E layer, the ionization of which is caused by other components of the solar radiation. In particular, soft X-ray 10–50 Å radiation is taken into account in modern D layer ionization models (Eccles et al., 2005; where it is taken into account using a solar spectrum model). The combined effect of increasing

absorption in the *E* layer and a slight refraction extending the path length in the absorbing layer leads to the need to take into account the ionization of the *E* layer.

To analyze the correlation of the noise attenuation with various solar radiation lines, we carried out a joint analysis of the absorption during the 80 flares of 2013–2017 and data from varied instruments, namely: GOES/XRS (Hanser & Sellers, 1996; Machol & Viereck, 2016), GOES/EUVS (Machol et al., 2016), SDO/AIA (Lemen et al., 2012), PROBA2/LYRA (Dominique et al., 2013; Hochedez et al., 2006), SOHO/SEM (Didkovsky et al., 2006), and SDO/EVE(ESP; Didkovsky et al., 2012). These instruments provide direct and regular observations of solar radiation in the wavelength range 1–2,500 *Å* during the period under study (see Table S2 in the supporting information for details). It is well known that at different wavelengths the solar radiation dynamics during flares is different (Donnelly, 1976). This allows us to find the solar radiation lines that most strongly influence the dynamics of the noise variations at the coherent radars.

To determine the effective ionization lines, we calculate the following probability:

$$P(\Lambda) = P\left(R(P(t), I_{\Lambda}(t)) \geq R(P(t), I_{1-8\forall}(t)) | R(P(t), I_{1-8\forall}(t)) \geq 0.4\right) \tag{10}$$

In this expression, $P(\Lambda)$ is the probability that the correlation coefficient $R(P(t), I_{\Lambda}(t))$ of the observed absorption $P(t)$ with the intensity $I_{\Lambda}(t)$ of a given solar radiation line Λ during the X-ray flare period will not be lower than the correlation coefficient $R(P(t), I_{1-8\mathring{A}}(t))$ of the observed absorption $P(t)$ with the intensity $I_{1-8\mathring{A}}(t)$ of GOES/XRS 1-8*Å* line. The calculations are carried out only for cases during which the correlation coefficient between absorption and GOES/XRS solar radiation is greater than 0.4.

It should be noted that if the distribution of values of the correlation coefficients are similar and independent for different wavelengths of solar radiation, then $P(\Lambda)$ should not exceed 0.5. Exceeding this level indicates a line of solar radiation to be a controlling factor for the attenuation of the noise. Figure 4b shows the results of this analysis based on the processing of over 11,977 individual observations.

One can see from Figure 4b that very often (in 62% to 68% of the cases) $P(\Lambda)$ exceeds 0.5 for Λ in the ranges SDO/AIA 94 *Å*, SDO/EVE 1–70 *Å*, 300–340 *Å*, SDO/AIA 304,335 *Å*, and SOHO/SEM 1–500 *Å*. This indicates the need to take these solar radiation lines into account when interpolating the HF noise attenuation. All these lines are absorbed below 150 km (Tobiska et al., 2008, Figure 2). They are therefore sources of ionization in the lower part of the ionosphere and are contributing to the radio noise absorption observed in the experiment.

Let us demonstrate the potential of using the linear combination of six lines from these spectral ranges (1–8, 94, 304, 335, 1–70, and 1–500 *Å*) instead of just single 1- to 8-*Å* GOES/XRS line. Let us assume that ionization is produced by different lines independently and linearly, and the contributions of each line to ionization are positive and are retrievable. Nonlinear case will be discussed later. To search for the amplitude of these contributions, we used the nonnegative least squares method (Lawson & Hanson, 1995). It provides an iterative search for the best approximation of experimental noise attenuation $P_{\text{att}}(t)$ by a linear combination of solar radiation dynamics at different wavelengths ($P_{1-8\mathring{A}}(t)$, $P_{94\mathring{A}}(t)$, $P_{304\mathring{A}}(t)$, $P_{335\mathring{A}}(t)$, $P_{1-70\mathring{A}}(t)$, and $P_{1-500\mathring{A}}(t)$) with unknown nonnegative weighting multipliers. In addition we also take into account slow background noise dynamics by adding a linear dependence $C_0 + C_1 t$ into the regression.

Finally, we search for parameters $C_{0..7}$ that solve the problem:

$$\int_{T_{flare}-1h}^{T_{\text{flare}}+2h} (P_{\text{att}}(t) - C_0 - C_1 t - C_2 P_{1-8\forall}(t) - C_3 P_{94\forall}(t) - C_4 P_{304\forall}(t) - C_5 P_{335\forall}(t) - C_6 P_{1-70\forall}(t) - C_7 P_{1-500\forall}(t))^2 \mathrm{d}t = \min \tag{11}$$

under the limitation that C_2, C_3, C_4, C_5, C_6, and C_7 be all positive.

Examples of approximations and statistical results are shown in Figures 4c–4l. It can be seen that the sum of four lines (dash-dotted green line) approximates the experimental data much better than just a single GOES/XRS (dotted black line) solar radiation line. Figure 4c shows the probability density function of the correlation coefficients when the experimental data are approximated by linear combinations of the lines 1–8, 94, 304, 335, 1–70, and 1–500 *Å*. The figure shows that the combination of the lines 1–8 and 94 *Å* (solid black line) fits the experimental data no worse than the combination of all six lines (dash-dotted green line), and significantly better than the single line 1–8 *Å* (dotted black line). This allows us to use a combination of

the two lines 1–8 and 94 Å as parameters of the noise attenuation model during X-ray solar flares at these radars.

In this paper we analyze only X-ray flares, and the level of Lyman-α line is comparatively weak. Therefore, the well-known dependence of the D layer ionization with Lyman-α is not detected (see Figure 4b).

Lines 10–100 Å are usually absorbed at heights of the order of and below 100 km (Banks & Kockarts, 1973, Figure 1.7, par.6.3.). This indicates a significant contribution of the lower part of the E layer to the noise absorption observed by the radars.

The median value of the correlation coefficient of the noise attenuation with 1–8 Å is 0.62, with the combination of 1- to 8-Å + 94-Å lines is 0.76, and with the combination of all six lines is 0.73.

Thus, taking into account the line 94 Å leads to an increase in the median correlation coefficient from 0.62 to 0.76, while adding other lines does not significantly increase the correlation. This allows us concluding that use of the 1- to 8- and 94-Å solar radiation lines as a proxy of the noise attenuation profile potentially allows a more accurate approximation of the temporal dynamics of the experimentally observed noise attenuation, and as a result, of the temporal dynamics of the absorption of the HF radio signals in the lower part of the ionosphere. Figures 4d–4l show the attenuation of HF noise dynamics when it is approximated only by GOES/XRS 1–8 Å (green dashed line) and by a combination of GOES/XRS 1–8Å and SDO/AIA 94 Å solar radiation (red line). The approximations are shown for several radars during several flares. It can be seen from the figure that taking into account intensity of the SDO/AIA 94-Å line significantly improve the accuracy of fitting the noise attenuation dynamics.

In the first approximation total absorption during X-ray solar flares depends on the square root of the weighted integral from the solar radiation intensity. It is seen in experiments (Schumer, 2010) and can be explained theoretically. Unfortunately, fitting the observed noise attenuation by the model:

$$P_{\text{att}}(t)[\text{dB}] \approx C_0 + C_1 t + (\sum_i B_i \cdot P_i(t))^{1/2} \tag{12}$$

(where P_i is intensity of ith line of solar radiation, and C_0, C_1, B_i are unknown coefficients) for taking into account several solar radiation lines is nonlinear problem. Therefore, in this case the solution requires complex and slow algorithms for carrying out automatic calculations, which is inconvenient for processing large amounts of data used in the paper. Therefore, above we used the simple linear approximation (11) of the model (12):

$$P_{\text{att}}(t)[\text{dB}] \approx C_0 + C_1 t + \sum_i B_i \cdot P_i(t), \tag{13}$$

which is faster in the calculations than the model (12). From a mathematical point of view, we can do this, since linear dependence on parameters is the first approximation of nonlinear dependencies and is associated with the possibility of decomposition of functions into Taylor series (Korn & Korn, 2013). Although from a physical point of view, this is not entirely correct; however, this allowed us to estimate the contribution of different wavelengths of solar radiation into noise attenuation and take into account their superposition in the first approximation.

To verify our conclusion about the necessity of taking into account the solar radiation both 1–8 Å and near 100 Å when analyzing the noise dynamics at 8–20 MHz, we carried out additional calculations. We made fitting by nonlinear approximation of the absorption model (12):

$$P_{\text{att}}(t)[\text{dB}] \approx C_0 + C_1 t + \sum_i B_i \cdot P_i^{1/2}(t) \tag{14}$$

The model (14) is linear in C_0, C_1, B_i and therefore fast enough for fit experimental data. Also it is closer to the theoretical dependence (12) than linear model (11) and (13). The results obtained for nonlinear model (Figure 5) using formulas similar to (10) and (11) produce results similar with linear model results (Figure 4). As one can see, in both cases a very good correlation is observed between noise attenuation and SDO/AIA 94Å line intensity (Figure 4b) and between noise attenuation and square root of intensity (Figure 5a). Fitting by SDO/AIA 94Å line together with standard GOES/XRS 1- to 8-Å line significantly increase the most probable correlation coefficient between model and experiment both for linear model and for nonlinear model

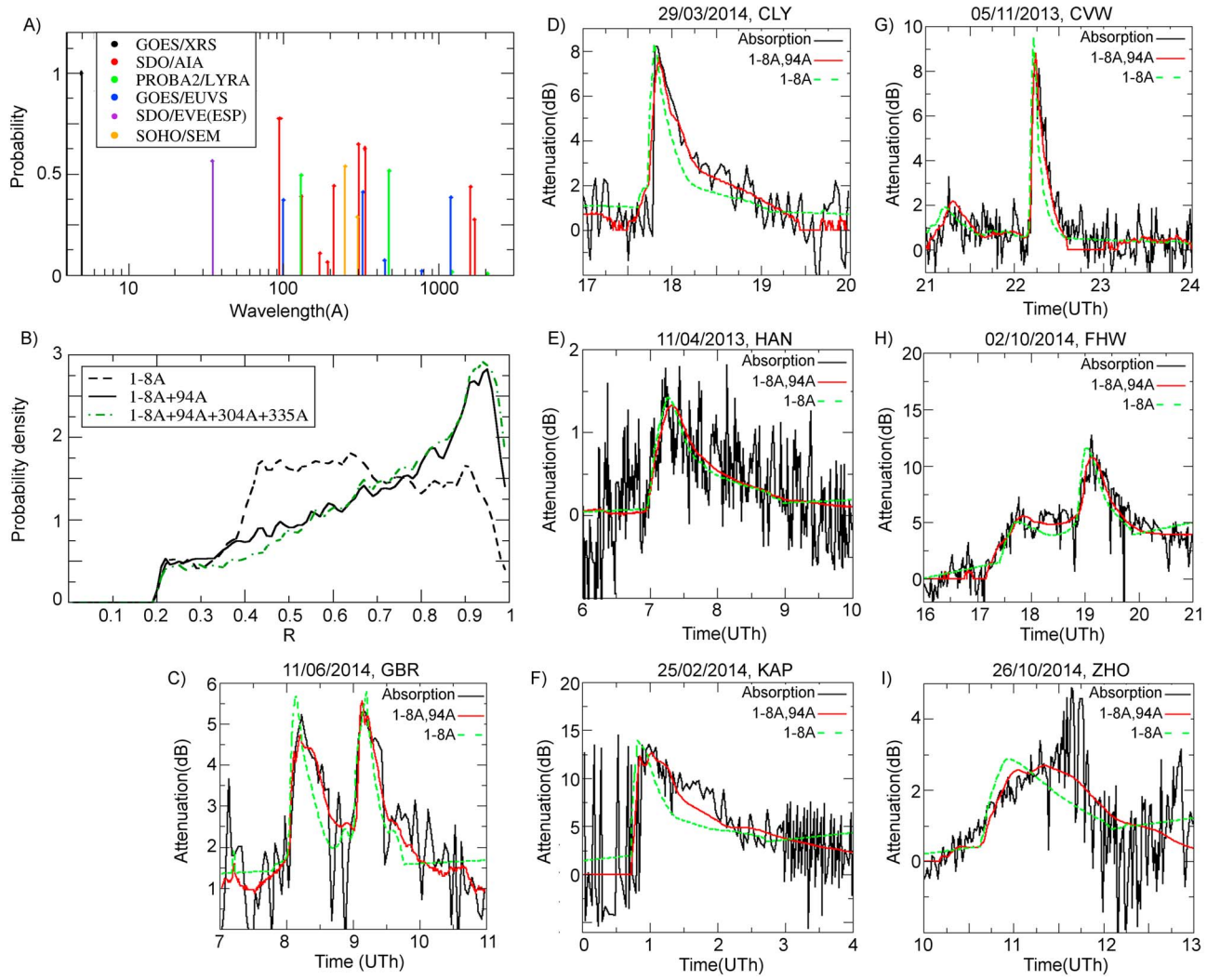

Figure 5. Statistical results for nonlinear model (14). (a) The probability $P(\Lambda)$ over all the flares and the radars. (b) Probability density function of correlation coefficients for various approximations of the noise absorption experimental data; (c–i) examples of fitting the attenuation of HF noise by different combinations of solar spectrum lines (at different radars during different X-ray flares).

(shown by black solid lines in Figures 4c and 5b) in comparison with fitting only by 1- to 8-*Å* line (shown by black dashed lines in Figures 4c and 5b). One can see that taking into account 94-*Å* line improves accuracy of fitting of the observed noise attenuation both by linear (Figures 4d–4l) and nonlinear (Figures 5c–5i) models.

Good correspondence between the results obtained by the two different approximations confirms our conclusion that it is important to take into account both wavelengths 1–8 *Å* and wavelengths near 100 *Å* for the analysis of ionospheric noise absorption at 8–20 MHz during X-ray solar flares. Therefore, it is necessary to take into account not only the *D* layer but also the *E* layer of the ionosphere for the interpretation of the noise absorption during X-ray solar flares. This corresponds well with the results obtained by Eccles et al. (2005).

5. Diagnostics of Global Absorption Effects

Taking into account all of the above, it is possible to build an automatic system suitable for global analysis of ionospheric absorption of HF radio waves over the area covered by radar field of views. The algorithm for constructing the automatic absorption analysis system consists of the following stages.

At the first stage, the GS signal range curve is determined from the daily behavior of the GS signal. We model the ionosphere as a parabolic layer of known half-thickness Δh and height h_{mF2}, but of unknown amplitude

$f_{oF2}(t)$ and dynamics. The temporal dynamics of $f_{oF2}(t)$ is approximated by the nonlinear parametric function (4), and its parameters are calculated from experimental data via a fitting procedure.

Using this GS signal range curve, the elevation angle of the received GS signal is estimated as a function of time. The location of the region making the main contribution to the absorption of the radio noise is found simultaneously. Its calculation is based on the Breit-Tuve principle (Davies, 1969) and on the assumption that the signal is reflected at the virtual height h_{mF2}. Such a calculation is carried out separately for each radar, for each beam. The algorithm for constructing the dynamics of GS range and the elevation angle is given above (1) and (3).

At the second stage, the noise absorption level $\tilde{P}_{vert,10\,\mathrm{MHz}}(t, \phi(t), \lambda(t))$ is estimated for the vertical radio wave propagation in the absorbing layer at a frequency of 10 MHz for each beam of the radar, at a geographical point $(\phi(t), \lambda(t))$ corresponding to the position of the effective absorbing region. It is calculated from the noise variations $\tilde{P}(t)$ detected by the radar, taking into account the elevation angle Θ_{model} of the radio signal propagation in the absorbing layer, which was calculated at the first stage using algorithm described above 3. The absorption corresponds to the geographic coordinates $(\phi(t), \lambda(t))$, also calculated in the first stage, and set to the point which is farthest away from the radar (the trajectory crosses D layer at two points). The observed dependence of absorption on frequency $f(t)$ is interpolated to 10-MHz frequency using our retrieved median frequency dependence. The resulting expression for the vertical absorption is

$$\tilde{P}_{\mathrm{vert,10\ \ MHz}}(t, \phi(t), \lambda(t)) = \tilde{P}(t)\sin(\Theta_{\mathrm{model}}(t))\left(\frac{f(t)}{f_0}\right)^{1.6} \tag{15}$$

where $f_0 = 10$ MHz, and $f(t)$ is the radar sounding frequency.

Figures 6a–6h show the absorption dynamics over the radars field of views during the 07 January 2014 solar flare based on the proposed algorithm. One can see the global-scale absorption effect between 18:18 and 19:12 UT that corresponds to the solar X-ray flare. Each radar produces several measurement points, corresponding to the number of beams, one beam – one measurement point. So the spatial resolution and resolved areas depend on radio wave propagation characteristics and could vary from flare to flare.

As shown by a preliminary analysis, the smallness of variations in the operational frequency of the radar within the studied time domain is important to reduce the algorithmic errors of this technique. It allows one to reduce errors related with the variability of noise level at different frequencies, but not with its absorption. Also, radars which have relatively low ionospheric noise level should be excluded from the analysis. Otherwise, the noise variations associated with the discretization errors of the analog signal are large, and this reduces the accuracy of the estimation of the absorption dynamics. Therefore, to demonstrate the method, we selected the radars that within 17–21 UT changed their operational frequency by no more than 300 kHz, and having maximum amplitude of ionospheric noise 20 dB above the digital noise level. Also, we use only the data that correspond to the calculated model ranges to the absorption point not exceeding 2,500 km. Green sectors in Figures 6a–6h correspond to the field of view of 16 radars that meet the criteria above and used to process the absorption data. As one can see, the obtained results demonstrate the dependence discussed earlier (Berngardt et al., 2018)—the main noise absorption is most often observed in the sunlit region. On the other hand, it is clear that only part of the radars (about half) operates in a sufficient mode for measurement—on the one hand they do not significantly change the operating frequencies, on the other hand, they have a sufficiently high noise level to study its dynamics. Figure demonstrates that most of the areas in which absorption diagnostics is possible are located polarward from the radars, at latitudes above 40°.

For future practical purposes one can fit the obtained absorption measurements over space by a smoothing function or join them with regular riometric measurements.

One of the ways to smooth the obtained data is through their accumulation over latitude or longitude. It allows us to more clearly distinguish the temporal dynamics of absorption and to reveal its average latitudinal or longitudinal dependencies.

Figure 6i shows the dynamics of median absorption as a function of latitude during this event. The median was calculated over 3 geographical degrees. Figure 6j shows the dynamics of median absorption as a function of longitude during this event. The median was calculated over 3 geographical degrees. For comparison solar radiation at 1–8 and 94$\mathring{A}$ is shown in Figure 6k. It can be seen from the figure that the proposed method

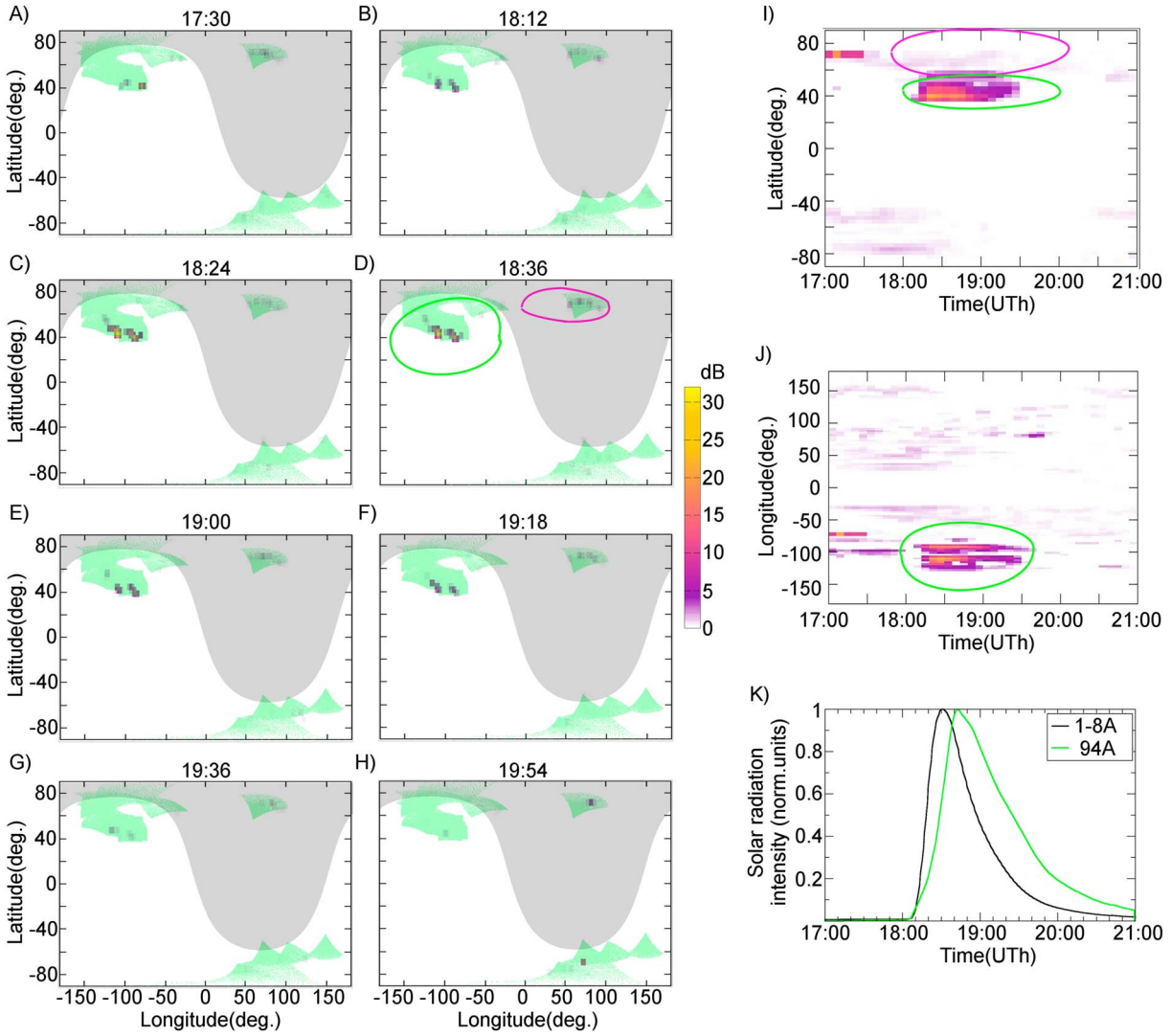

Figure 6. (a–h) Vertical absorption dynamics at 10 MHz during solar X-ray flare X1.2 07 January 2014 according to the radar network and model (15). Gray region marks unlit area at 100-km height. Green regions marks field of views of the radars, involved into measurements. (i) Latitude absorption dynamics during the flare, median over all the longitudes; (j) longitude absorption dynamics during the flare, median over all the latitudes; (k) the intensity of solar radiation from the data of GOES/XRS 1–8 *Å* and SDO/AIA 94 *Å*. Color scale is the same for panels (a)–(j). Green and violet regions mark effects in lit and unlit conditions.

makes it possible to investigate the spatiotemporal dynamics of absorption over a significant part of the Earth's surface.

A joint analysis of Figures 6a–6j allows, for example, to distinguish absorption regions in the lit area that correlate well with the flare (green regions) from the effects in the unlit area that can not be correctly interpreted with the approach taken in this paper.

Thus, the results obtained in this paper allow us to state with a high degree of confidence that the daytime noise absorption observed during X-ray flares at 8–20 MHz occurs at the heights of the *D* and *E* layers, at the distance of the first hop. Previous studies (Berngardt et al., 2018; Bland et al., 2018) with a subset of SuperDARN radars did not reach this conclusion. The use of an automatic algorithm for estimating the elevation angle and range to GS allows localizing the absorption region, unlike previous studies (Berngardt et al., 2018; Bland et al., 2018). The results obtained in the paper allow one to interpret the observed noise attenuation at radar frequency (shown, e.g., in Figure 1) in terms of equivalent vertical absorption at a fixed frequency (10 MHz; shown, e.g., in Figure 6) using (15).

Acknowledgments
The authors acknowledge the use of SuperDARN data, which are freely available through the SuperDARN website at Virginia Polytechnic Institute and State University (http://vt.superdarn.org/). The data of the SuperDARN radars were obtained using the DaViT (https://github.com/vtsuperdarn/davitpy). The authors are grateful to all the developers of the DaViT system, in particular K.Sterne, N.Frissel, S. de Larquier, and A.J.Ribeiro, as well as to all the organizations supporting the radars operation. O. B. is grateful to X. Shi (Virginia Tech) for help in using DaViT. In the paper we used the data of EKB ISTP SB RAS, operating under financial support of FSR Program II.12.2. The data of EKB ISTP SB RAS radar are available at ISTP SB RAS (http://sdrus.iszf.irk.ru/ekb/page_example/simple). The authors acknowledge the use of SuperDARN data. SuperDARN is a collection of radars funded by the national scientific funding agencies of Australia, Canada, China, France, Italy, Japan, Norway, South Africa, United Kingdom, and the United States. The SuperDARN Kerguelen radar is operated by IRAP (CNRS and Toulouse University) and is funded by IPEV and CNRS through INSU and PNST programs. The Dome C East radar was installed in the framework of a French-Italian collaboration and is operated by INAF-IAPS with the support of CNR and PNRA. The SuperDARN SENSU Syowa East and South radars are the property of National Institute of Polar Research (NIPR); this study is a part of the Science Program of Japanese Antarctic Research Expedition (JARE) and is supported by NIPR under Ministry of Education, Culture, Sports, Science and technology (MEXT), Japan. The SuperDARN Canada radar operations (SAS, PGR, INV, RKN, and CLY) are supported by the Canada Foundation for Innovation, the Canadian Space Agency, and the Province of Saskatchewan. The authors thank SuperDARN Canada for providing the data from the two-frequency operating modes. The authors are grateful to Altyntsev A. T., Tashchilin A. V., Kashapova L. K. (ISTP SB RAS) for useful discussions. The authors are grateful to NOAA for GOES/XRS and GOES/EUVS data (available at https://satdat.ngdc.noaa.gov/sem/goes/data), to NASA/SDO and to the AIA and EVE teams for SDO/AIA and SDO/EVE data (available at https://sdo.gsfc.nasa.gov/data/, http://lasp.colorado.edu/eve/data_access/service/file_download/, and http://suntoday.lmsal.com/suntoday/), to Royal Observatory of Belgium for PROBA2/LYRA data (available at http://proba2.oma.be/

Thus, the system that we have constructed can be used for studies of spatiotemporal features of daytime absorption both as a separate network and with other instruments and techniques.

6. Conclusion

In the present work, a joint analysis was carried out of the data of 35 HF over-the-horizon radars (34 SuperDARN radars and the EKB ISTP SB RAS radar) during 80 solar flares of 2013–2017. The analysis shows the following features of the absorption of 8- to 20-MHz radio noise.

The position of an effective noise source on the ground and the error in determining its location can be determined by the position of spatial focusing at the boundary of the dead zone and the form of this focusing (GS signal). This allows using the GS signal to estimate the position of the region that makes the main contribution to the observed absorption of the HF radio noise at a particular radar frequency. The program code is available at Berngardt (2019).

The analysis of the correlation between different solar radiation lines and HF noise dynamics has shown that the temporal variation of the absorption is well described by a linear combination of the solar radiation intensity at the wavelengths 1–8 $\mathring{A}$ measured by GOES/XRS and at the wavelength of 94 $\mathring{A}$ measured by SDO/AIA. This allows us to conclude that the main absorption is caused by ionospheric D and E layers. The assumption we used in our paper about a linear superposition of the contributions of each solar line to absorption is relatively rough. To solve more accurately for the reconstruction of the electron density profile from the experimentally observed noise absorption and from the solar spectrum, it is necessary to take into account the processes of ionization by the various radiation components and corresponding delays more correctly, for example, following the approach of Eccles et al. (2005).

The frequency dependence of the HF absorption is determined by the median dependence $A[\mathrm{dB}] \sim f^{-1.6\pm0.3}$.

A model and algorithms are constructed (15), which provides automatic radar estimates of vertical daytime absorption at 10 MHz. Using these model algorithms, it is possible to make statistical analysis and case studies of the spatiotemporal dynamics of the absorption of HF radio waves globally, within the coverage area of radar field of views. Each radar produces several measurement points, corresponding to the number of beams, one beam – one measurement point. So the spatial resolution and resolved areas depend on radio wave propagation characteristics and will vary from flare to flare.

One important problem with the algorithm constructed here is the determination of the geographical location of the absorption region during the day. This location depends on whether the most intense 1-hop absorption is located near the radar or near the GS distance of the first hop. A similar problem arises with the URSI A1 method. For future applications, one might want to fit the retrieved absorption measurements through the use of a smoothing function over space. However, at night or near the terminator, this algorithm should not be used.

Another problem of the algorithm is the impossibility of taking into account irregular variations in the background ionosphere. This is important for a more correct estimation of ray trajectory and, as result, for more accurate estimation of the vertical absorption from the experimental data for specific observations. The use of calibrated experimental measurements of the ray elevation angles of GS signals and new techniques for identifying GS signals from radar data should help to solve this problem in the future.

References

Akmaev, R. A. (2010). DRAP model validation: I. Scientific report. https://www.ngdc.noaa.gov/stp/drap/DRAP-V-Report1.pdf

Bailey, K. D. (1994). *Typologies and taxonomies: An introduction to classification techniques*, Quantitative Applications in the Social Sciences. Thousand Oaks, CA: SAGE Publications.

Baker, J. B. H., Greenwald, R. A., Ruohoniemi, J. M., Oksavik, K., Gjerloev, J. W., Paxton, L. J., & Hairston, M. R. (2007). Observations of ionospheric convection from the Wallops SuperDARN radar at middle latitudes. *Journal of Geophysical Research*, *112*, A01303. https://doi.org/10.1029/2006JA011982

Banks, P. M., & Kockarts, G. (1973). *Aeronomy* (Vol. A). New York and London: Academic Press.

Berngardt, O. I. (2019). berng/sdGsRange: Initial. https://doi.org/10.5281/zenodo.2576653

Berngardt, O. I., Ruohoniemi, J. M., Nishitani, N., Shepherd, S. G., Bristow, W. A., & Miller, E. S. (2018). Attenuation of decameter wavelength sky noise during X-ray solar flares in 2013–2017 based on the observations of midlatitude HF radars. *Journal of Atmospheric and Solar-Terrestrial Physics*, *173*, 1–13.

Berngardt, O. I., Zolotukhina, N. A., & Oinats, A. V. (2015). Observations of field–aligned ionospheric irregularities during quiet and disturbed conditions with EKB radar: First results. *Earth, Planets and Space*, *67*(1), 143.

lyra/data/bsd/) used for analysis. The authors are grateful to the University of Southern California Space Sciences Center for using SOHO/SEM data (available at https://dornsifecms.usc.edu/space-sciences-center/download-sem-data/). Solar Heliospheric Observatory (SOHO) is a joint mission project of United States National Aeronautics and Space Administration (NASA) and European Space Agency (ESA). LYRA is a project of the Centre Spatial de Liege, the Physikalisch-Meteorologisches Observatorium Davos and the Royal Observatory of Belgium funded by the Belgian Federal Science Policy Office (BELSPO) and by the Swiss Bundesamt für Bildung und Wissenschaft. A. S. Y. is supported by Japan Society for the Promotion of Science (JSPS), "Grant-in-Aid for Scientific Research (B)" (Grant 25287129). J. M. R. acknowledges the support of NSF through award AGS-1341918. O. I. B. is supported by RFBR grant 18-05-00539a.

Bilitza, D., Altadill, D., Truhlik, V., Shubin, V., Galkin, I. A., Reinisch, B. W., & Huang, X. (2017). International Reference Ionosphere 2016: From ionospheric climate to real–time weather predictions. *Space Weather*, *15*, 418–429. https://doi.org/10.1002/2016SW001593

Blagoveshchenskii, D. V., Maltseva, O. A., Anishin, M. M., Rogov, D. D., & Sergeeva, M. A. (2015). Modeling of HF propagation at high latitudes on the basis of IRI. *Advances in Space Research*, *57*(3), 821–834.

Blanchard, G. T., Sundeen, S., & Baker, K. B. (2009). Probabilistic identification of high–frequency radar backscatter from the ground and ionosphere based on spectral characteristics. *Radio Science*, *44*, RS5012. https://doi.org/10.1029/2009RS004141

Bland, E. C., Heino, E., Kosch, M. J., & Partamies, N. (2018). SuperDARN radar–derived HF radio attenuation during the September 2017 solar proton events. *Space Weather*, *16*, 1455–1469. https://doi.org/10.1029/2018SW001916

Bliokh, P. V., Galushko, V. G., Minakov, A. A., & Yampolski, Y. M. (1988). Field interference structure fluctuations near the boundary of the skip zone. *Radiophysics and Quantum Electronics*, *31*(6), 480–487.

Chakraborty, S., Ruohoniemi, J. M., Baker, J. B. H., & Nishitani, N. (2018). Characterization of short–wave fadeout seen in daytime SuperDARN ground scatter observations. *Radio Science*, *53*, 472–484. https://doi.org/10.1002/2017RS006488

Chernov, Y. A. (1971). *Backward–oblique sounding of the ionosphere (in Russian)*. Moscow, USSR: Moscow, Svyaz.

Chisham, G. (2018). Calibrating SuperDARN interferometers using meteor backscatter. *Radio Science*, *53*, 761–774. https://doi.org/10.1029/2017RS006492

Chisham, G., Lester, M., Milan, S. E., Freeman, M. P., Bristow, W. A., McWilliams, K. A., et al. (2007). A decade of the Super Dual Auroral Radar Network (SuperDARN): scientific achievements, new techniques and future directions. *Surveys in Geophysics*, *28*, 33–109.

DRAP Documentation (2010). Global D–region absorption prediction documentation, accessed September,2018. https://www.swpc.noaa.gov/content/global-d-region-absorption-prediction-documentation

Davies, K. (1969). *Ionospheric radio waves*, Blaisdell book in the pure and applied sciences: Waltham, MA: Blaisdell Pub. Co.

Detrick, D. L., & Rosenberg, T. J. (1990). A phased–array radiowave imager for studies of cosmic noise absorption. *Radio Science*, *25*(4), 325–338.

Didkovsky, L. V., Judge, D. L., Jones, A. R., Wieman, S., Tsurutani, B. T., & McMullin, D. (2006). Correction of SOHO CELIAS/SEM EUV measurements saturated by extreme solar flare events. *Astronomische Nachrichten*, *328*(1), 36–40.

Didkovsky, L. V., Judge, D., Wieman, S., Woods, T., & Jones, A. (2012). EUV SpectroPhotometer (ESP) in Extreme Ultraviolet Variability Experiment (EVE): Algorithms andăcalibrations. *Solar Physics*, *275*(1), 179–205.

Dominique, M., Hochedez, J.-F., Schmutz, W., Dammasch, I. E., Shapiro, A. I., Kretzschmar, M., et al. (2013). The LYRA instrument onboard PROBA2: Description and in-flight performance. *Solar Physics*, *286*(1), 21–42.

Donnelly, R. F. (1976). Empirical models of solar flare X ray and EUV emission for use in studying their E and F region effects. *Journal of Geophysical Research*, *81*(25), 4745–4753.

Eccles, J. V., Hunsucker, R. D., Rice, D., & Sojka, J. J. (2005). Space weather effects on midlatitude HF propagation paths: Observations and a data–driven D region model. *Space Weather*, *3*, S01002. https://doi.org/10.1029/2004SW000094

Fiori, R. A. D., Koustov, A. V., Chakraborty, S., Ruohoniemi, J. M., Danskin, D. W., Boteler, D. H., & Shepherd, S. G. (2018). Examining the potential of the Super Dual Auroral Radar Network for monitoring the space weather impact of solar X–ray flares. *Space Weather*, *16*, 1348–1362. https://doi.org/10.1029/2018SW001905

Galkin, I. A., Reinisch, B. W., Huang, X., & Bilitza, D. (2012). Assimilation of GIRO data into a real–time IRI. *Radio Science*, *47*, RS0L07. https://doi.org/10.1029/2011RS004952

Greenwald, R. A., Baker, K. B., Dudeney, J. R., Pinnock, M., Jones, T. B., Thomas, E. C., et al. (1995). Darn/Superdarn: A global view of the dynamics of high–latitude convection. *Space Science Reviews*, *71*, 761–796.

Hall, G. E., MacDougall, J. W., Moorcroft, D. R., St.-Maurice, J.-P., Manson, A. H., & Meek, C. E. (1997). Super Dual Auroral Radar Network observations of meteor echoes. *Journal of Geophysical Research*, *102*(A7), 14,603–14,614.

Hanser, F. A., & Sellers, F. B. (1996). Design and calibration of the GOES–8 solar X–ray sensor: The XRS. *Proceedings of the SPIE*, *2812*, 344–352.

Hargreaves, J. K. (2010). Auroral radio absorption: The prediction question. *Advances in Space Research*, *45*(9), 1075–1092.

Hochedez, J.-F., Schmutz, W., Stockman, Y., Schühle, U., Benmoussa, A., Koller, S., et al. (2006). LYRA, a solar UV radiometer on Proba2. *Advances in Space Research*, *37*, 303–312.

Hunsucker, R. D., & Hargreaves, J. K. (2002). *The high–latitude ionosphere and its effects on radio propagation*, Cambridge atmospheric and space science series. Cambridge: Cambridge University Press.

ITU-R P.372-13 (2016). Recommendation ITU-R P.372-13. Radio noise. https://www.itu.int/rec/R-REC-P.372-13-201609-I/en

Korn, G. A., & Korn, T. M. (2013). *Mathematical handbook for scientists and engineers: Definitions, theorems, and formulas for reference and review*, Dover Civil and Mechanical Engineering. New York: Dover Publications. https://books.google.ru/books?id=A4XCAgAAQBAJ

Lawal, H. A., Lester, M., Cowley, S. W. H., Milan, S. E., Yeoman, T. K., Provan, G., et al. (2018). Understanding the global dynamics of the equatorial ionosphere in Africa for space weather capabilities: A science case for AfrequaMARN. *Journal of Atmospheric and Solar-Terrestrial Physics*. https://doi.org/10.1016/j.jastp.2018.01.008

Lawson, C., & Hanson, R. (1995). *Solving least squares problems*. Philadelphia, PA: Society for Industrial and Applied Mathematics.

Lemen, J. R., Title, A. M., Akin, D. J., Boerner, P. F., Chou, C., Drake, J. F., et al. (2012). The Atmospheric Imaging Assembly (AIA) on the Solar Dynamics Observatory (SDO). *Solar Physics*, *275*(1), 17–40.

Machol, J., & Viereck, R. (2016). GOES X–ray Sensor (XRS) Measurements. https://www.ngdc.noaa.gov/stp/satellite/goes/doc/GOES_XRS_readme.pdf

Machol, J., Viereck, R., & Jones, A. (2016). GOES EUVS Measurements. https://www.ngdc.noaa.gov/stp/satellite/goes/doc/GOES_NOP_EUV_readme.pdf

Oinats, A. V., Nishitani, N., Ponomarenko, P., Berngardt, O. I., & Ratovsky, K. G. (2016). Statistical characteristics of medium–scale traveling ionospheric disturbances revealed from the Hokkaido East and Ekaterinburg HF radar data. *Earth, Planets and Space*, *68*(1), 8.

Pederick, L. H., & Cervera, M. A. (2014). Semiempirical Model for Ionospheric Absorption based on the NRLMSISE–00 atmospheric model. *Radio Science*, *49*, 81–93. https://doi.org/10.1002/2013RS005274

Ponomarenko, P. V., Iserhienrhien, B, & St.-Maurice, J.-P. (2016). Morphology and possible origins of near-range oblique HF backscatter at high and midlatitudes. *Radio Science*, *51*, 718–730. https://doi.org/10.1002/2016RS006088

Ponomarenko, P., Nishitani, N., Oinats, A. V., Tsuya, T., & St.-Maurice, J.-P. (2015). Application of ground scatter returns for calibration of HF interferometry data. *Earth, Planets and Space*, *67*(1), 138.

Ponomarenko, P. V., St.-Maurice, J.-P., Hussey, G. C., & Koustov, A. V. (2010). HF ground scatter from the polar cap: Ionospheric propagation and ground surface effects. *Journal of Geophysical Research*, *115*, A10310. https://doi.org/10.1029/2010JA015828

Ribeiro, A. J., Ruohoniemi, J. M., Baker, J. B. H., Clausen, S., de Larquier, S., & Greenwald, R. A. (2011). A new approach for identifying ionospheric backscatter in midlatitude SuperDARN HF radar observations. *Radio Science*, *46*, RS4011. https://doi.org/10.1029/2011RS004676

Ribeiro, A. J., Ruohoniemi, J. M., Baker, J. B. H., Clausen, L. B. N., Greenwald, R. A., & Lester, M. (2012). A survey of plasma irregularities as seen by the midlatitude Blackstone SuperDARN radar. *Journal of Geophysical Research*, *117*, A02311. https://doi.org/10.1029/2011JA017207

Rogers, N. C., & Honary, F. (2015). Assimilation of real–time riometer measurements into models of 30 MHz polar cap absorption. *Journal of Space Weather and Space Climate*, *5*, A8.

Sauer, H. H., & Wilkinson, D. C. (2008). Global mapping of ionospheric HF/VHF radio wave absorption due to solar energetic protons. *Space Weather*, *6*, S12002. https://doi.org/10.1029/2008SW000399

Schumer, E. A. (2010). Improved modeling of midlatitude D–region ionospheric absorption of high frequency radio signals during solar X–ray flares (PhD dissertation), Air Force Institute of Technology.

Shearman, E. D. R. (1956). A study of ionospheric propagation by means of ground back–scatter. *Proceedings of the IEE - Part B: Radio and Electronic Engineering*, *103*(8), 203–209.

Shepherd, S. G. (2017). Elevation angle determination for SuperDARN HF radar layouts. *Radio Science*, *52*, 938–950. https://doi.org/10.1002/2017RS006348

Simon, D. (2013). *Evolutionary Optimization Algorithms*. New Jersey: Wiley.

Squibb, C. O., Frissell, N. A., Ruohoniemi, J. M., Baker, J. B. H., Fiori, R., & Moses, M. L. (2015). Dayside Ionospheric Response to X–Class Solar Flare Events Observed with Reverse Beacon Network High Frequency Communication Links. In *Virginia tech reu symposium – poster presentation, Book of abstracts, 113–113*. Blacksburg, VA, Virginia Tech REU Program.

Stocker, A. J., Arnold, N. F., & Jones, T. B. (2000). The synthesis of travelling ionospheric disturbance (TID) signatures in HF radar observations using ray tracing. *Annales Geophysicae*, *18*(1), 56–64.

Tobiska, K. W., Bouwer, D. S., & Bowman, B. R. (2008). The development of new solar indices for use in thermospheric density modeling. *Journal of Atmospheric and Solar-Terrestrial Physics*, *70*(5), 803–819.

Uryadov, V. P., Vertogradov, G. G., Sklyarevsky, M. S., & Vybornov, F. I. (2018). Positioning of Ionospheric Irregularities and the Earth's Surface Roughness Using an Over-the-Horizon HF Radar. *Radiophysics and Quantum Electronics*, *60*, 688–702.

Warrington, E. M., Stocker, A. J., Siddle, D. R., Hallam, J., Al-Behadili, H. A. H., Zaalov, N. Y., et al. (2016). Near real–time input to a propagation model for nowcasting of HF communications with aircraft on polar routes. *Radio Science*, *51*, 1048–1059. https://doi.org/10.1002/2015RS005880

Watanabe, D., & Nishitani, N. (2013). Study of ionospheric disturbances during solar flare events using the SuperDARN Hokkaido radar. *Advances in Polar Science*, *24*(1), 12–18.

Yukimatu, A. S., & Tsutsumi, M. (2002). A new SuperDARN meteor wind measurement: Raw time series analysis method and its application to mesopause region dynamics. *Geophysical Research Letters*, *29*(20), 1981. https://doi.org/10.1029/2002GL015210